

[Progress in Ultrafast Intense Laser Science](#)

Volume V

Bearbeitet von
Antonio Giulietti, Kenneth Ledingham

1. Auflage 2009. Buch. xv, 212 S. Hardcover
ISBN 978 3 642 03824 2
Format (B x L): 15,5 x 23,5 cm
Gewicht: 550 g

[Weitere Fachgebiete > Physik, Astronomie > Elektrodynamik, Optik > Quantenoptik,
Nichtlineare Optik, Laserphysik](#)

schnell und portofrei erhältlich bei


DIE FACHBUCHHANDLUNG

Die Online-Fachbuchhandlung beck-shop.de ist spezialisiert auf Fachbücher, insbesondere Recht, Steuern und Wirtschaft. Im Sortiment finden Sie alle Medien (Bücher, Zeitschriften, CDs, eBooks, etc.) aller Verlage. Ergänzt wird das Programm durch Services wie Neuerscheinungsdienst oder Zusammenstellungen von Büchern zu Sonderpreisen. Der Shop führt mehr als 8 Millionen Produkte.

Coherent Lattice Oscillations in Solids and Their Optical Control

Part I. Fundamentals and Optical Detection Techniques

Kunie Ishioka and Oleg V. Misochko

Summary. Coherent optical phonons are the lattice atoms vibrating in phase with each other over a macroscopic spatial region. With sub-10 fs laser pulses, one can impulsively excite the coherent phonons of a frequency up to 50 THz, and detect them optically as a periodic modulation of electric susceptibility. The generation and relaxation processes depend critically on the coupling of the phonon mode to photoexcited electrons. Real-time observation of coherent phonons can thus offer crucial insight into the dynamic nature of the coupling, especially in extremely nonequilibrium conditions under intense photoexcitation.

2.1 Introduction

Illumination of light on solids leads to electron-hole pair excitation if the photon energy exceeds the bandgap. The photoexcited carriers cool down in femto- to picoseconds, first by distributing the excess energy among themselves and then by transferring the energy to the lattice sub-system. The latter process has been extensively studied in semiconductors by time-resolved Raman spectroscopy. Because Raman scattering requires a nearly monochromatic incident light, the time-resolution has been limited to the picosecond range.

With development of ultrashort pulsed lasers, coherently generated lattice dynamics was found, first as the periodic modulation in the transient grating signal from perylene in 1985 by De Silvestri and coworkers [1]. Shortly later, similar modulation was observed in the reflectivity of Bi and Sb [2] and of GaAs [3], as well as in the transmissivity of YBCO [4] by different groups. Since then, the coherent optical phonon spectroscopy has been a simple and powerful tool to probe femtosecond lattice dynamics in a wide range of solid

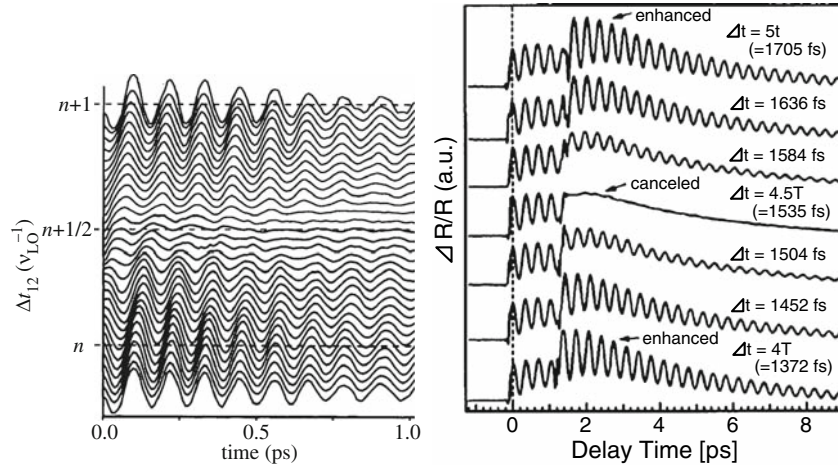


Fig. 2.1. Double-pump and probe reflectivity signal of coherent LO phonons of GaAs (*left*) and coherent A_{1g} phonons of Bi (*right*). The horizontal axis gives the time delay of the probe pulse with respect to the first pump pulse in both panels. Δt_{12} (Δt) in the *left* (*right*) panel is the time delay between the two pump pulses in units of the LO phonon period $\nu_{LO}^{-1}=114 \text{ fs}$ (A_{1g} phonon period $T = 341 \text{ fs}$). From [5] and [6]

materials. The coherent optical phonons are generated only during the illumination of femtosecond optical pulses, in contrast to hot incoherent phonons created during hot carrier cooling for picoseconds. They are coherent in the sense that two time-separated optical pulses can enhance or destroy the oscillation depending on the separation between the pulses (Fig. 2.1). In contrast to coherent acoustic phonons propagating as ballistic strain pulses in crystals, the coherent phonons of optical branches are nonpropagating and delocalized, as light couples directly with phonons only at the Γ point of the Brillouin zone ($k=0$) where the group velocity is nearly zero.

This and the next chapters give an overview of the recent experimental researches on coherent optical phonons. The generation mechanism and the optical detection techniques are described in Sects. 2.2 and 2.3 of this chapter, respectively, followed by the findings of the optical experiments in a variety of solid materials in Sects. 2.4–2.7. The next chapter presents the non-optical detection techniques and their findings in Sect. 3.1, together with the achievements of the optical control experiments in Sect. 3.2. As we would like to stress recent developments in limited pages, we omit many classical works on which the readers can refer to the excellent reviews on ferroelectrics [7,8], GaAs and its heterostructures [9,10], π -conjugated chains [11], dihalogen-doped rare gas crystals [12] and quasi-1D halogen-bridged metal complexes [13], and surface phonons [14,15].

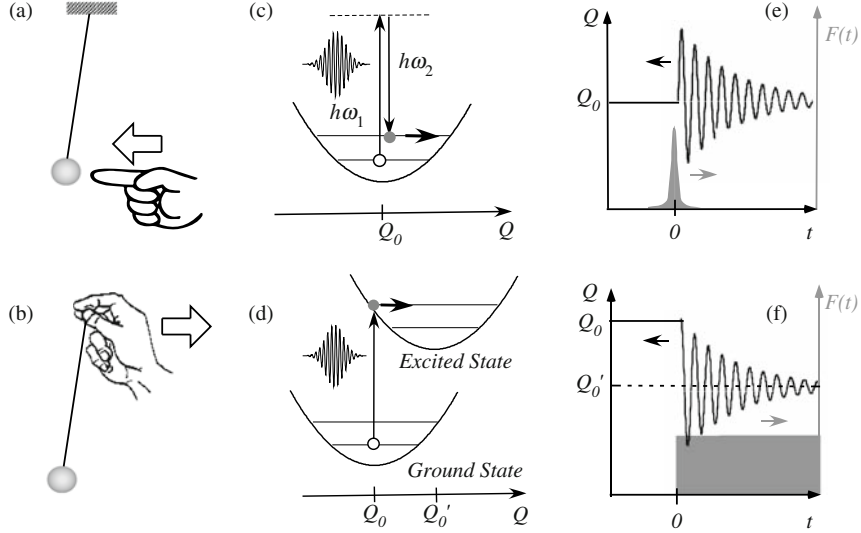


Fig. 2.2. Two generation models of coherent optical phonons. (a), (c), (e) impulsive stimulated Raman scattering (ISRS). (b), (d), (f) displacive excitation of coherent phonons (DECP). Graphs (e) and (f) display the time evolution of the driving force (*grey areas*) and that of the displacement (*solid curves*) for ISRS and DECP, respectively

2.2 Generation of Coherent Phonons

The classical equation of motion¹ describing the coherent phonons for a small nuclear displacement Q is that of a driven harmonic oscillator [9, 10, 15]

$$\mu \left[\frac{\partial^2 Q(t)}{\partial t^2} + 2\gamma \frac{\partial Q(t)}{\partial t} + \omega_0^2 Q(t) \right] = F(t), \quad (2.1)$$

with the reduced lattice mass μ , the damping γ and the frequency ω . The generation mechanism of the coherent phonons can be classified into two types, “impulsive” and “displacive,” according to the temporal-profile and the origin of the force $F(t)$. The impulsive excitation is realized with a δ -function-like driving force created via stimulated Raman scattering (Fig. 2.2 c, e). Displacive excitation is achieved by a step-function-like force via a potential shift in the excited state (Fig. 2.2 d, f).

2.2.1 Impulsive Stimulated Raman Scattering

Up to now, only Raman active modes at the Γ point of the Brillouin zone have been observed as coherent phonons in bulk crystals.² The selection rule can be

¹ Quantum description of coherent vibrations is given in [7, 15, 16].

² Exceptions include coherent IR-active (but Raman-inactive) phonons observed as a THz emission from Te [17] and CdTe [18].

partly explained in terms of impulsive stimulated Raman scattering (ISRS) [7, 15, 19] in the generation process, illustrated in Fig. 2.2c for a nonresonant case. A broadband optical pulse can offer multiple combinations of two photons whose energy difference matches the vibrational energy ($h\omega_1 - h\omega_2 = h\omega_0$), and give an impulsive driving force to initiate coherent nuclear motion on the ground electronic state. This situation is an analogue of giving a kick to a weight of a pendulum and changing its kinetic energy (Fig. 2.2a). The driving force is defined by the Raman polarizability [9, 15]

$$F(t) = \frac{1}{2} \left(\frac{\partial \alpha}{\partial Q} \right)_{kl} E_k E_l. \quad (2.2)$$

The key requirements for ISRS excitation are the existence of Raman active phonons in the crystal, and the pulse duration shorter than the phonon period ω_0^{-1} [19]. The resulting nuclear oscillation follows a sine function of time (i.e., minimum amplitude at $t=0$), as shown in Fig. 2.2e. ISRS occurs both under nonresonant and resonant excitations. As the Raman scattering cross section is enhanced under resonant excitation, so is the amplitude of the ISRS-generated coherent phonons.

Experimental verification of the ISRS generation can be primarily given by the pump polarization dependence. The coherent phonons driven by ISRS (second order process) should follow the symmetry of the Raman tensor, while those mediated by photoexcited carriers should obey the polarization dependence of the optical absorption (first order process). It is possible, however, that both ISRS and carrier-mediated generations contribute to the generation of a single phonon mode. The polarization dependence is then described by the sum of the first- and second-order processes [20–22], as shown in Fig. 2.3.

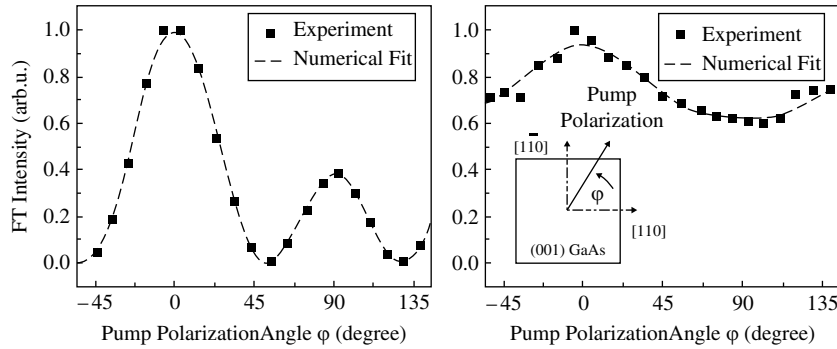


Fig. 2.3. The Fourier-transformed (FT) intensity of coherent phonons as a function of the pump polarization angle φ for a GaAs/Al_{0.36}Ga_{0.64}As MQW. The excitation wavelength is slightly above the $n=1$ exciton resonance (*left*) and slightly above the $n=2$ subband energy (*right*). φ -dependent component is attributed to ISRS, while the φ -independent component is to TDFS and forbidden Raman scattering. From [20]

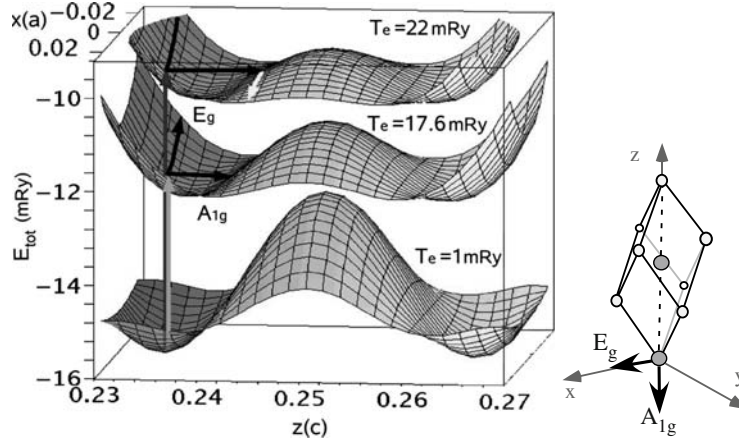


Fig. 2.4. *Left:* potential energy surfaces calculated for the ground state ($T_e = 1$ mRy) and for excited electronic states ($T_e = 17.6$ and 22 mRy) of Bi. *Vertical arrows* show transitions of the atoms from the ground state to an excited energy surface. From [23]. *Right:* crystalline structure of Bi and Sb crystals. The directions of the A_{1g} and E_g modes are indicated in both panels

2.2.2 Photocarrier-Mediated Excitation of Coherent Phonons

Early pump-probe experiments on semimetals Bi and Sb by Cheng and coworkers detected only the fully symmetric (A_{1g}) mode but not the other Raman active (E_g) mode [2,24]. The apparent absence of the E_g mode³ led the authors to propose an alternative generation mechanism: displacive excitation of coherent phonons (DECP) [27]. In DECP, a sudden shift of the vibrational potential kick-starts the coherent oscillation on the electronic excited state (Fig. 2.2d). The shift in the equilibrium coordinate ($Q'_0(t) - Q_0$) is assumed to be a linear function of the photoexcited electron density $n(t)$. This situation is analogous to quickly translating the suspension point of a pendulum and thereby changing the potential energy (Fig. 2.2b). The requirements for DECP generation are such electron-phonon coupling that shifts the potential energy surface by electronic excitation, and the pulse duration shorter than the phonon period. The resulting nuclear oscillation is a cosine function of time (i.e., maximum amplitude at $t = 0$), as shown in Fig. 2.2f.

The DECP model successfully explained the observed initial phase of the fully symmetric phonons in a number of opaque crystals [24]. The absence of the E_g mode was attributed to an exclusive coupling between the electrons photoexcited near the Γ point and the fully symmetric phonons. A recent density functional theory (DFT) calculation [23] demonstrated this exclusive coupling as the potential energy surface (Fig. 2.4). The minimum of the potential surface of the excited state shifted significantly along the trigonal (z) axis,

³ Coherent E_g phonon was later observed experimentally in Bi [6,25] and Sb [26].

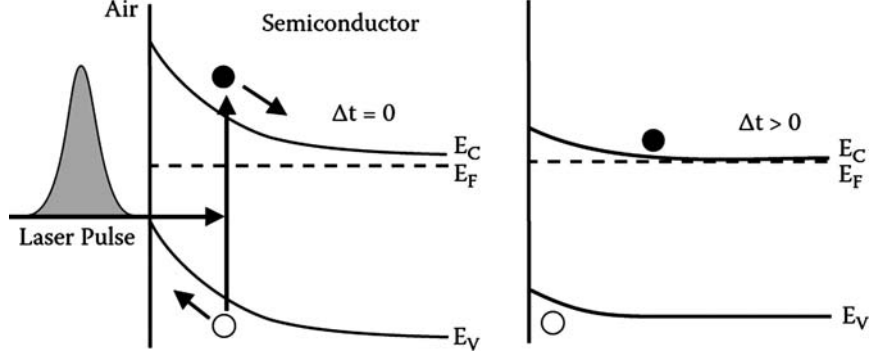


Fig. 2.5. Schematic sketch of transient depletion field screening (TDFS) in an n-doped semiconductor with midgap Fermi-level pinning at the surface. Excitation of free electron–hole pairs leads to rapid drift currents on the time scale of the exciting laser pulse (*left*). After the excitation, electrons and holes are spatially separated and the space charge field is screened (*right*). From [10]

that is, the direction of the A_{1g} mode, because it is the direction of the Peierls distortion. In contrast, the minimum shifts very little in the direction of the E_g mode, which is perpendicular to the direction of the Peierls distortion.

As the lattice interacts with light only through electrons, both DECP and ISRS should rely on the electron–phonon coupling in the material. Distinction between the two models lies solely in the nature of the electronic transition. In this context, Merlin and coworkers proposed DECP to be a resonant case of ISRS with the excited state having an infinitely long lifetime [26, 28]. This original “resonant ISRS” model failed to explain different initial phases for different coherent phonon modes in the same crystal [21, 25]. Recently, the model was modified to include finite electronic lifetime [29] to have more flexibility to reproduce the experimental observations.

In polar semiconductors, carrier-mediated generation occurs in the form of transient depletion field screening (TDFS) depicted in Fig. 2.5 [30]. The driving force in (2.1) can be expressed by the sum of the Raman term and the nonlinear longitudinal polarization [10]:

$$F_j(t) = \frac{1}{2} \left(\frac{\partial \alpha}{\partial Q} \right)_{kl} E_k E_l - \frac{e^*}{\epsilon_\infty \epsilon_0} P_j^{NL}. \quad (2.3)$$

The nonlinear polarization can be divided into several different contributions:

$$P_j^{NL} = \chi_{jkl}^{(2)} E_k E_l + \chi_{jklm}^{(3)} E_k E_l E_m + \int_{-\infty}^t dt' J_j(t') + Ne \int_{-\infty}^t dt' \int_{-\infty}^{\infty} dx_j \langle \Psi(x_j, t') | x_j | \Psi(x_j, t') \rangle. \quad (2.4)$$

The third term describes the polarization set up by ultrafast drift-diffusion currents, which can excite coherent phonons via TDFS (or via the buildup of electric Dember fields [9, 10]). The first two terms represent the second- and the third-order nonlinear susceptibilities, respectively [31]. The fourth term describes the polarization associated with coherent electronic wavefunctions, which becomes important in semiconductor heterostructures.

For surface coherent phonons of ferromagnetic metals, a spin-driven generation mechanism was proposed, as will be described in Sect. 2.6.

2.3 Optical Detection of Coherent Phonons

Optical detection offers the most conventional technique to time-resolve the coherent phonons. It includes four-wave mixing [8], transient reflectivity [9, 10] and transmission [7] measurements, as well as second harmonic generation (SHG) [15, 32]. Coherent nuclear displacement Q induces a change in the optical properties (e.g., reflectivity R) of the crystal through the refractive index n and the susceptibility χ ,

$$\Delta R = \frac{\partial R}{\partial n} \Delta n \approx \frac{\partial R}{\partial \chi} \frac{\partial \chi}{\partial Q} Q(t), \quad (2.5)$$

which makes ΔR to be a quantitative, though not absolute, measure for Q . Because $\partial \chi / \partial Q$ is a first-order Raman tensor, only Raman active modes with nonzero $\partial \chi / \partial Q$ can be detected by linear optical detection [9, 10].

Figure 2.6 illustrates an experimental setup for pump-probe reflectivity measurements. In the standard reflectivity measurements, the reflected probe light is detected without polarization analysis. In this scheme, coherent phonons of any symmetry can in principle be detected, given the polarizations of the pump and probe beams appropriately chosen. By contrast, the “anisotropic” scheme, often referred to as “electro-optic (EO) sampling” [33], detects only the anisotropic component of the reflectivity arising from non-fully symmetric phonons. It employs probe beam polarized at 45° with respect to the optical plane, and detection of the difference of the s - and p -polarized components of the reflected probe beam ($\Delta R_p - \Delta R_s$) with a pair of matched photodiodes, as illustrated in Fig. 2.6. Another technique illustrated is the fast scan, in which the signal is stored and averaged in a digital oscilloscope while the pump-probe delay is continuously scanned. This enables an averaging of the signal over 1,000 times in a minute, and thus improves the signal-to-noise ratio drastically. With these techniques combined, one can detect a reflectivity change as small as $\Delta R/R \sim 10^{-6}$.

By using a nonlinear optical process such as SHG, one can probe surface phonons and adsorbate-related vibrations exclusively [14, 15, 32, 34]. Time-resolved SHG (TRSHG) detects the second harmonic (SH) of the probe beam as a function of time delay between pump and probe. The SH electric field is driven by the nonlinear polarization $P_i(2\omega)$ at the surface, which

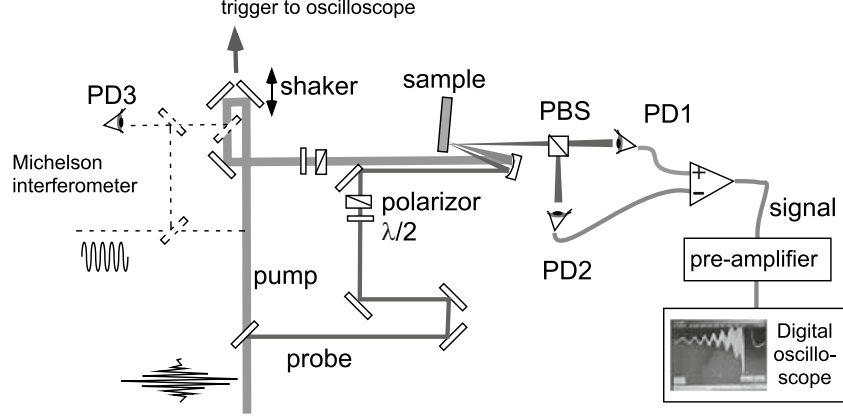


Fig. 2.6. Schematic illustration of the experimental setup for pump-probe anisotropic reflectivity measurements with fast scan method. PBS denotes polarizing beam splitter, PD1 and PD2, a pair of matched photodiodes to detect p - and s -polarized components of the reflected probe beam, PD3 another photodiode to detect the interference pattern of He-Ne laser in a Michelson interferometer to calibrate the scanning of the pump path length

can be expanded to the first order of the nuclear displacement $Q_{n,q}$ for the n -th phonon mode with wave vector q [14]:

$$P_i(2\omega) = [\chi_{ijk}^{(2)}(2\omega) + \sum_{n,q} (\partial\chi_{ijk}^{(2)}(2\omega)/\partial Q_{n,q})_0 Q_{n,q}] \times E_j(\omega)E_k(\omega). \quad (2.6)$$

The SH intensity is proportional to $|P|^2$. Experimentally, the oscillatory part of the total SH is so small that one can ignore its second-order term. If coherent surface phonons are created by ISRS, the whole process including excitation and detection is the coherent time-domain analogue of stimulated hyper Raman scattering ($\chi^{(4)}$ process) [14]. The cross section of the SHG process is then proportional to the product of a Raman tensor in the pump transition and a hyper-Raman tensor $\partial\chi_{ijk}^{(2)}/\partial Q_n$ in the probe transition.

2.4 Electron-Phonon Coupling in Group V Semimetals

Semimetals bismuth (Bi) and antimony (Sb) have been model systems for coherent phonon studies. They both have an A7 crystalline structure and sustain two Raman active optical phonon modes of A_{1g} and E_g symmetries (Fig. 2.4). Their pump-induced reflectivity change, shown in Fig. 2.7, consists of oscillatory (ΔR_{osc}) and non-oscillatory (ΔR_{nonosc}) components. ΔR_{osc} is dominated by the coherent nuclear motion of the A_{1g} and E_g symmetries, while ΔR_{nonosc} is attributed to the modification in the electronic and the lattice temperatures.

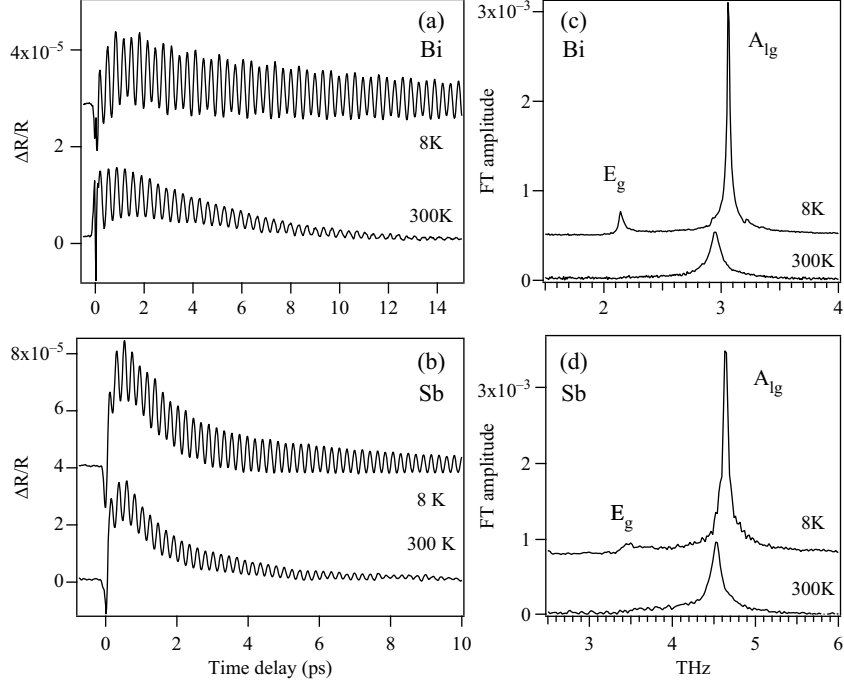


Fig. 2.7. (a, b): transient reflectivity changes $\Delta R/R$ of Bi and Sb single crystals at different temperature. (c, d): FT spectra of the oscillatory component $\Delta R_{osc}/R$. The excitation pulse energy is $9 \mu\text{J}/\text{cm}^2$ for Bi and $56 \mu\text{J}/\text{cm}^2$ for Sb. The traces are offset for clarity. Adapted from [25] and [21]

The coherent oscillation of the A_{1g} mode was a cosine function of time (Fig. 2.8) [21, 24–26]. Recent X-ray measurements demonstrated a clear shift in the equilibrium position at photoexcitation [35], as we will see in the next chapter. These results confirmed the displacive generation of coherent A_{1g} phonons, as discussed in Sect. 2.2.2. In contrast, the coherent oscillation of the E_g mode was a sine function of time, and its amplitude exhibited a $\cos 2\varphi$ dependence on the pump polarization angle φ . Both features indicated the ISRS generation of the coherent E_g phonons [21, 25].

Under moderate ($\mu\text{J}/\text{cm}^2$) photoexcitation, where the photoexcited carrier density is comparable or less than the intrinsic density, time evolution of coherent A_{1g} and E_g phonons is respectively described by a damped harmonic oscillation

$$Q(t) \propto \frac{\Delta R_{osc}}{R} = A_0 \exp(-\Gamma_0 t) \sin(\omega_0 t + \delta), \quad (2.7)$$

with the dephasing rate Γ_0 and the frequency ω_0 being independent of the photoexcitation density [21, 25]. Under intense (mJ/cm^2) photoexcitation, in contrast, both the A_{1g} and E_g phonons dephased faster, and their

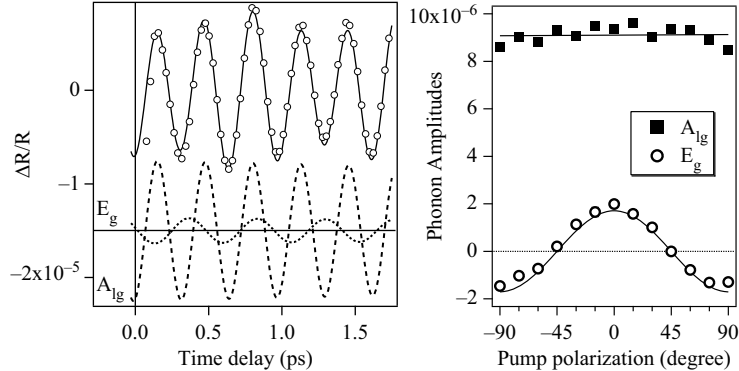


Fig. 2.8. *Left:* oscillatory part of the reflectivity change of Bi (0001) surface at 8K (*open circles*). Fit to the double damped harmonic function (*solid curve*) shows that the A_{1g} and E_g components (*broken and dotted curves*) are a sine and a cosine functions of time, respectively. *Right:* pump polarization dependence of the amplitudes of coherent A_{1g} and E_g phonons of Bi (0001). Adapted from [25]

frequencies redshifted, with increasing excitation density [36–38]. In this strong-excitation regime, the coherent phonons are better described as *chirped* damped oscillations

$$\frac{\Delta R_{\text{osc}}}{R} = A_0 \exp(-\Gamma_0 t) \sin((\omega_0 + \alpha t)t + \delta), \quad (2.8)$$

with the frequency varying at a positive rate α with time delay (Fig. 2.9). The origin of the redshift was first attributed to the lattice anharmonicity by Hase and coworkers [36], but later double-pulse experiments [39] combined with DFT calculations [40] by Murray and coworkers attributed it to the electronic softening. In fact, the redshift in the frequency and the increase in the dephasing rate can be understood in terms of a Fano interference between two paths: one directly from the discrete (phonon) state and another mediated by a (electronic) continuum [38, 41]. The interference leads to an asymmetric line shape in the frequency domain given by

$$f(\epsilon) = \frac{(\epsilon + q)^2}{1 + \epsilon^2}, \quad (2.9)$$

with q being the asymmetry parameter and ϵ the dimensionless energy. The parameter q is a function of the phonon self-energy, whose real and imaginary parts correspond to the bare phonon frequency and the broadening, respectively. Its temperature- and pump power-dependences indicated that the continuum includes both the lattice and electronic degrees of freedom [38]. The contribution of the lattice anharmonicity was also confirmed by the observation of the two-phonon combination modes (e.g., $A_{1g} - E_g$ and $A_{1g} + E_g$) in the experiment [42] and theory [23], though the electronic softening undoubtedly plays a substantial role.

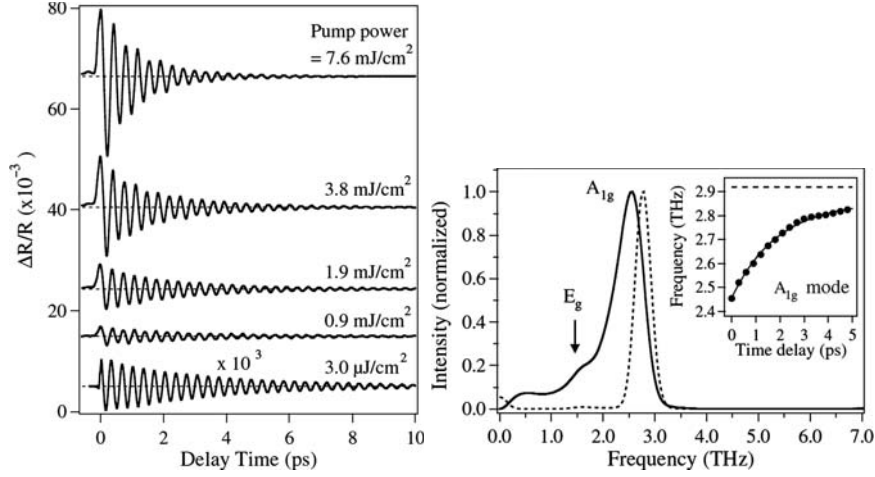


Fig. 2.9. *Left:* transient reflectivity change of Bi at various pump densities. *Right:* discrete wavelet transformation spectra obtained for time delay of 0.3 ps (*solid line*) and 3.0 ps (*dotted line*). Inset in right panel shows the A_{1g} frequency as a function of the time delay. The *dashed line* in inset represents the equilibrium frequency. From [36]

Under even more intense photoexcitation ($\sim 10 \text{ mJ/cm}^2$), the coherent A_{1g} and E_g phonons of Bi and Sb exhibit a collapse-revival in their amplitudes (Fig. 2.10) [42,43]. This phenomenon has a clear threshold in the pump density, which is common for the two phonon modes but depends on temperature and the crystal (Bi or Sb). At first glance, the amplitude collapse-revival appears to be analogous to the fractional revival in nuclear wavepackets in molecules [44, 45]. However, the pump power dependence may be an indication of a polarization, not quantum, beating between different spatial components of the coherent response within the laser spot [46].

2.5 Coherent Phonons in Group IV Crystals and Graphitic Materials

2.5.1 Coherent Phonons in Tetrahedrally Bonded Crystals

Silicon is a model for the fundamental electronic and mechanical properties of Group IV crystals and the basic material for electronic device technology. Coherent optical phonons in Si revealed the ultrafast formation of “renormalized” quasiparticles in time-frequency space [47]. The anisotropic transient reflectivity of n-doped Si(001) featured the coherent optical phonon oscillation with a frequency of 15.3 THz, when the [110] crystalline axis was parallel to the pump polarization (Fig. 2.11). Rotation of the sample by 45° led to disappearance of the coherent oscillation, which confirmed the ISRS generation,

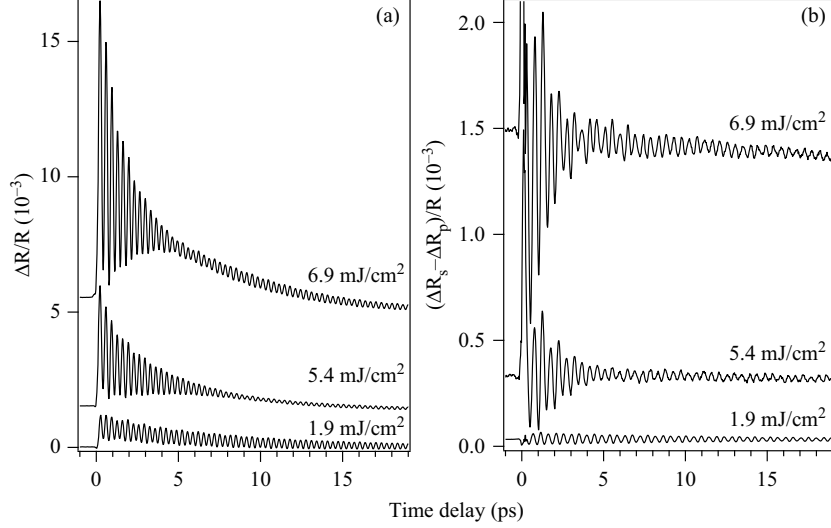


Fig. 2.10. Transient reflectivity change $\Delta R/R$ (a) and its anisotropic component $(\Delta R_p - \Delta R_s)/R$ (b) from Bi (0001) at 8 K for different pump densities. Pump polarization is chosen to show only the coherent A_{1g} or E_g phonons, respectively

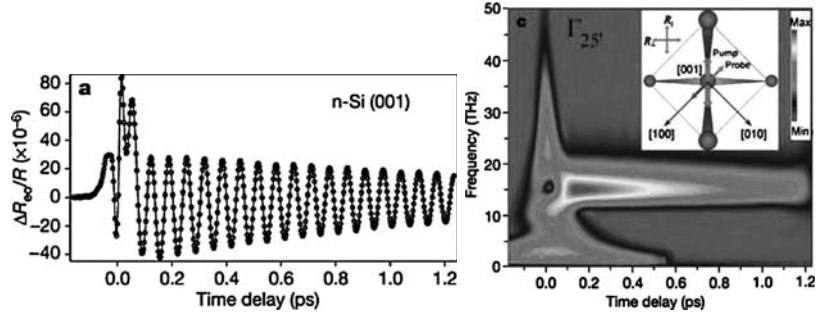


Fig. 2.11. Transient anisotropic reflectivity change for Si(001) in the $\Gamma_{25'}$ geometry (left) and its continuous wavelet transform (right). Inset in the right panel defines the polarization of the pump beam relative to the crystalline axes. From [47]

like in Ge [48]. Time-dependent spectral amplitude (chronogram) in Fig. 2.11 revealed the fast broadband response near $t = 0$ due to the coherent electronic coupling of the pump and probe fields via the nonlinear susceptibility. The optical phonon was seen at 15.3 THz for all the time delay $t > 0$. The most intriguing aspect of the chronogram was the anti-resonance at 15.3 THz slightly after $t = 0$, suggesting the coherent excitation of coupled phonon-carrier systems via electronic Raman process possibly near the Γ point and along the A direction. The data in Fig. 2.11 revealed interference effects leading to the coherent phonon generation and subsequent “dressing” by electron-hole

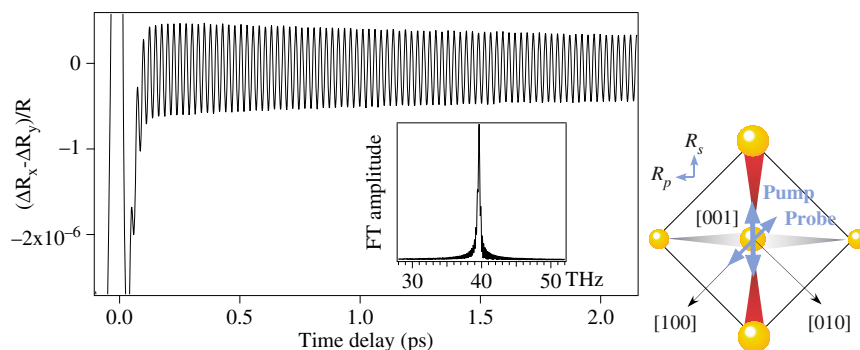


Fig. 2.12. *Left:* transient anisotropic reflectivity change of the (001) surface of single crystal type IIa diamond. Inset shows the FT spectrum of the oscillation, demonstrating a narrow peak of the optical phonon at 40 THz. *Right:* pump and probe polarizations to detect the optical phonon. Adapted from [50]

pairs. They clearly demonstrated the possibility of observing the quantum mechanical manifestations of carrier–phonon interactions in the real time, which until now could only be deduced from transport measurements and spectral lineshape analysis.

Isotope superlattices of nonpolar semiconductors gave an insight on how the coherent optical phonon wavepackets are created [49]. High-order coherent confined optical phonons were observed in $^{70}\text{Ge}/^{74}\text{Ge}$ isotope superlattices. Comparison with the calculated spectrum based on a planar force-constant model and a bond polarizability approach indicated that the coherent phonon amplitudes are determined solely by the degree of the atomic displacement, and that only the Raman active odd-number-order modes are observable.

Diamond has the widest bandgap among the group IV crystals. The anisotropic reflectivity change of diamond was modified at a period of 25 fs (frequency of 40 THz) when the pump polarization was parallel to the [110] direction (Fig. 2.12) [50]. The oscillatory signal essentially vanished after rotating the sample by 45° , as in Si [47] and Ge [48], which confirms the Raman generation. The dephasing rate of the optical phonon was obtained to be $\Gamma_0 = 0.145 \text{ ps}^{-1}$, giving a very large Q factor of ~ 300 . The amplitude of the coherent oscillation showed a linear pump power dependence. It clearly indicated the off-resonance, field-driven nature of the coherent phonon generation with 3.1 eV photons, whose energy was much smaller than the indirect (5.48 eV) or direct (7.3 eV) bandgaps.

2.5.2 Ultrafast Electron–Phonon Decoupling in Graphite

Graphite possesses highly anisotropic layered crystal structure, which translates to a quasi-2D electronic structure with electronic bands dispersing linearly near E_F and forming point-like Fermi surfaces. Visible light induces

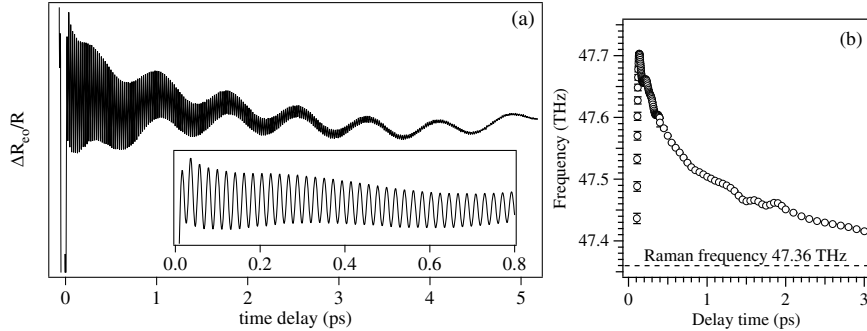


Fig. 2.13. (a) Anisotropic reflectivity change of graphite measured with sub-10 fs pulses at 3.1 eV. (b) Time evolution of the E_{2g2} phonon frequency obtained from time-windowed FT. From [51]

vertical transitions from the valence (π) to the conduction (π^*) bands near the K point of the Brillouin zone. Anisotropic reflectivity change of graphite (Fig. 2.13a) was modulated at two disparate periods of 21 and 770 fs, assigned to the in-plane carbon stretching (Raman G peak) [51] and the interlayer shear mode [52], respectively. The amplitudes of both phonons exhibited a $\cos 2\varphi$ dependence on the pump polarization angle φ , confirming their ISRS generation.

The coherent in-plane (E_{2g2}) phonon of graphite has a frequency of 47 THz. A time-windowed FT analysis (Fig. 2.13b) revealed that the phonon frequency blue-shifted promptly at the photoexcitation [51], contrary to the coherent phonon response in Bi, Sb (Sect. 2.4), Zn or Zr (Sect. 2.6). The recovery of the frequency to its near-equilibrium value (47.36 THz) took several picoseconds. The time scale, corresponding to those of carrier thermalization and carrier-lattice equilibration, suggests that the frequency shift is dominated by the excited electron dynamics. A DFT calculation demonstrated that non-adiabaticity plays an essential role in the phonon stiffening [51]. For unexcited graphite, the E_{2g2} phonon at the Γ point is softened due to electronic screening (a Kohn anomaly). For photoexcited graphite, the screening is weakened because the excited electrons near the E_F cannot follow the fast in-plane nuclear motion. Thus, the non-adiabatic electron-phonon decoupling leads to the stiffening of the E_{2g2} phonon without changing the bond length.

The coherent interlayer shear (E_{2g1}) phonon has a frequency as low as 1.3 THz (42 cm^{-1}), which makes the phonon mode a difficult target for CW Raman scattering but ideal for the time-resolved measurements. The frequency of the E_{2g1} phonon showed a red-shift upon heating to room temperature, but the dephasing rate had no significant temperature dependence [52]. The latter result suggested that the dephasing of this low-frequency phonon is dominated by coupling with electrons and/or defects. Under intense photoexcitation, the E_{2g1} phonon exhibited an amplitude collapse-revival (Fig. 2.14) [53], which looked similar to the collapse-revival in Bi and Sb (Fig. 2.10).

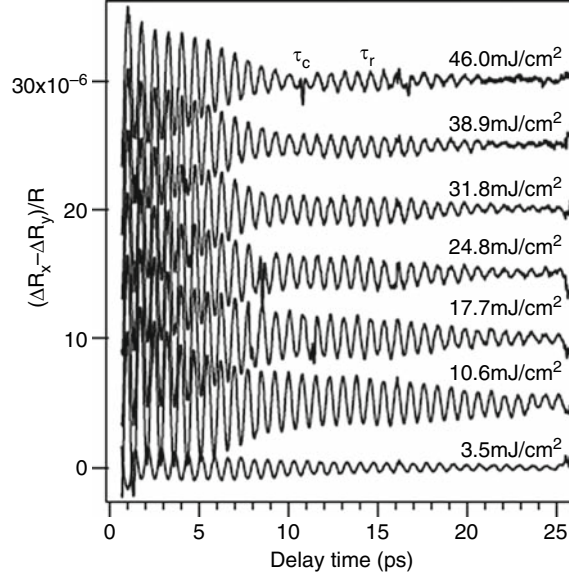


Fig. 2.14. Oscillatory part of the anisotropic reflectivity change of graphite under intense photoexcitation with 140 fs pulses at 1.55 eV at 7 K. From [53]

2.5.3 Exciton–Phonon and Phonon–Phonon Couplings in Carbon Nanotubes

With a structure of rolled up graphene sheets, carbon nanotubes (CNTs) have much in common in their electronic and phonon properties with those of graphite, for example, the linearly dispersing band structure near E_F and the Raman G peak at $\sim 1,600 \text{ cm}^{-1}$. Yet, extensive experimental and theoretical studies have found clear evidence of quantum size effects in CNTs. CNTs sustain the Raman active radial breathing modes (RBMs), whose frequency gives a good measure of their diameter. The tangential modes, which contribute to the Raman G peak, can split into different symmetries depending on the chirality.

Transient transmittance of single-walled carbon nanotubes (SWNTs) in suspension was modulated at two periods of ~ 140 and 21 fs, corresponding to the RBM and G mode, respectively [54, 55]. The amplitude and the frequency of the coherent RBMs exhibited a clear excitation-wavelength dependence (Fig. 2.15) [54]. The different frequencies were attributed to SWNTs with different diameters coming to the excitonic resonance. The FT spectra of the coherent RBMs in Fig. 2.15 had noticeable differences from the resonant Raman spectra, such as the different intensities and better frequency resolution.

The most striking feature of the coherent G mode was the periodic modulation in its frequency (Fig. 2.16) [55]. As the modulation period coincided

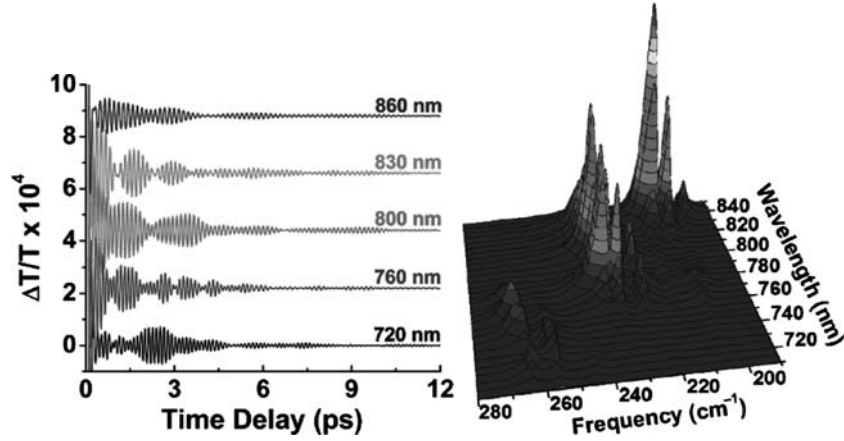


Fig. 2.15. *Left:* oscillatory part of the transient transmittance of SWNTs in a suspension excited and measured with 50 fs pulses at different photon energies. *Right:* a 3D plot of its FT spectrum obtained over a photon energy range of 1.746–1.459 eV (wavelength of 710–850 nm). From [54]

with that of the RBM, a straightforward interpretation was given in terms of the anharmonic coupling between the G mode and RBM on the excited excitonic state. The FT spectrum of the transient transmission signal gave almost equally spaced sidebands around the relatively sharp G peak at $1,588\text{ cm}^{-1}$, while the Raman spectrum of the same sample consisted of broad G and D bands. Quantum chemical modeling showed that the frequency modulation was due to a corrugation of the SWNT surface on photoexcitation, leading to a coupling between the longitudinal and radial vibrations in the excited state.

2.6 Coherent Optical Phonons in Metals

When metals have Raman active phonons, optical pump-probe techniques can be applied to study their coherent dynamics. Hase and coworkers observed a periodic oscillation in the reflectivity of Zn and Cd due to the coherent E_{2g} phonons (Fig. 2.17) [56]. The amplitude of the coherent phonons of Zn decreased with raising temperature, in accordance with the photo-induced quasi-particle density n_p , which is proportional to the difference in the electronic temperature before and after the photoexcitation (Fig. 2.17). The result indicated the resonant nature of the ISRS generation of coherent phonons. Under intense (mJ/cm^2) photoexcitation, the coherent E_g phonons of Zn exhibited a transient frequency shift similar to that of Bi (Fig. 2.9), which can be understood as the Fano interference [57]. A transient frequency shift was also observed for the coherent transverse optical (TO) phonon in polycrystalline Zr film, in spite of much weaker photoexcitation [58].

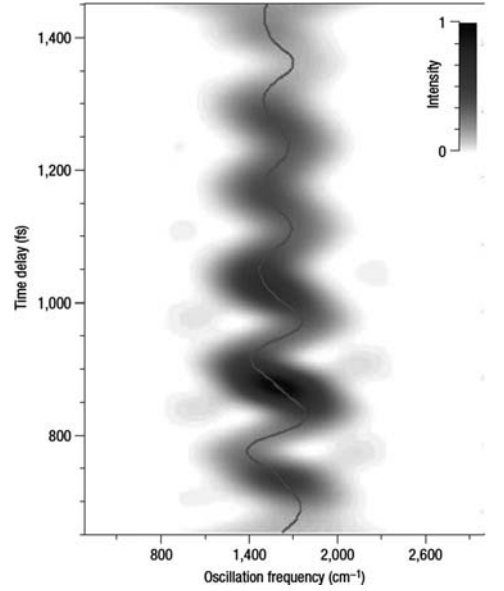


Fig. 2.16. G-mode frequency of SWNTs as a function of pump-probe time delay obtained from transient transmission measurement using a sub-10 fs pulse at 2.1 eV. From [55]

Coherent optical phonons from ferromagnetic systems attract interests in the context of ultrafast magnetic switching. SH signals from Gd(0001) surface in a magnetic field presented a previously unknown phonon–magnon coupled mode at 3 THz under resonant excitation of majority and minority spin subsystems (Fig. 2.18) [32, 59–61]. The frequency of the oscillation suggested the Γ_{3+} interlayer phonon mode at the surface. The vibration modifies the interaction of the spins in the adjacent layers significantly, and thus leads to the observed periodic modulation of the magnetization at the phonon frequency [60]. Above the Curie temperature T_C , the amplitudes of the coherent phonons of Gd(0001) and Tb(0001) did not depend on temperature significantly (Fig. 2.19), and the coherent phonon generation was attributed to DECP as introduced in Sect. 2.2.2. Below T_C , the amplitudes increased remarkably with a dependence that resembled the magnetization itself, indicating the coherent phonon excitation related to the ferromagnetic order [59]. One can consider a vibrational potential depending on the interlayer distance through the exchange interaction (spin) as well as the electron density (charge). If photo-induced spin-flip contributes to an additional shift in the potential minimum, the coherent phonons can be induced displacively by the spins. The damping rate of the coherent phonons for Gd and Tb increased monotonically with temperature, but close to T_C it was strongly reduced [59, 62]. The result indicated that phonon–magnon scattering dominates the

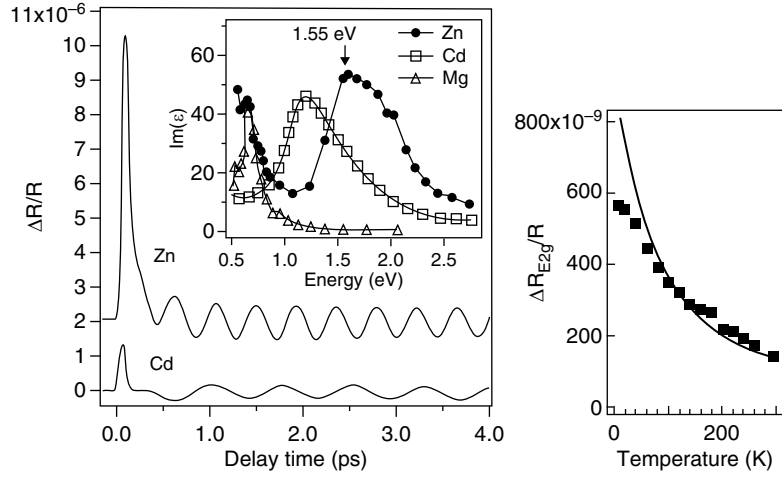


Fig. 2.17. *Left:* transient reflectivity change of Zn and Cd at 7 K. Inset shows the imaginary part of the dielectric function of Zn, Cd, and Mg. *Right:* amplitude of the coherent E_{2g} phonon of Zn as a function of temperature. *Solid curve* in the right panel represents the fit to n_p . From [56]

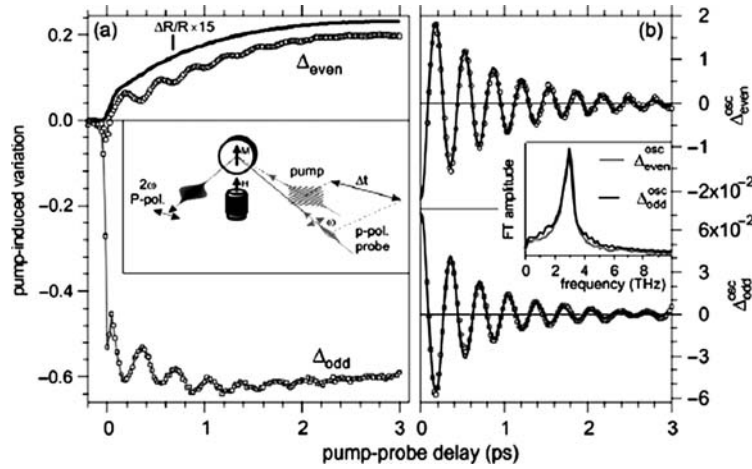


Fig. 2.18. (a) The even (*upper panel*) and odd (*lower panel*) SH responses of a 20 nm Gd(0001) film at 90 K using 815 nm/35 fs laser pulses. Transient reflectivity change is also displayed in the upper panel (*solid black curve*). The inset shows the experimental scheme with the magnetization oriented perpendicular to the plane of incidence. (b) The oscillatory part of the even and odd SH fields extracted from (a). The inset shows the corresponding FT spectra. From [59]

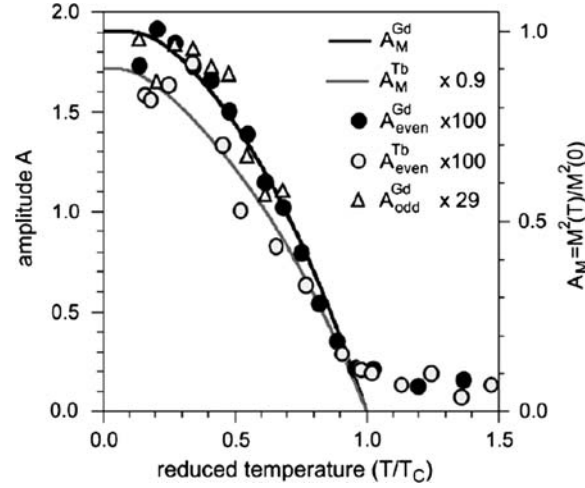


Fig. 2.19. Temperature dependence of the amplitudes of coherent phonons of Gd(0001) and Tb(0001). On the right axis, A_M^{Gd} and A_M^{Tb} show the square of calculated spontaneous magnetization given by the Brillouin function with $J_{\text{Gd}}=7/2$ and $J_{\text{Tb}}=6/2$ representing the magnetic moment of 4f electrons. From [59]

damping of the coherent phonons below T_C , together with phonon–phonon scattering and scattering by hot electrons.

2.7 Coherent Phonons in Other Materials

Coherent optical phonons and LO phonon–plasmon coupled (LOPC) modes have been investigated extensively in bulk III–V semiconductors, as well as on their surfaces and in their heterostructures. References [9, 10, 14] give comprehensive reviews of the experimental achievements, together with theoretical descriptions. Recently, Chang and coworkers confirmed that plasmons couple with both $A_1(\text{LO})$ $E_1(\text{LO})$ phonons to form LOPC modes in wurzite InN, and estimated the electron effective mass from the LOPC frequency [63, 64]. Hase estimated the electron mobility in GaAs by making use of the carrier density-dependence of the LOPC frequency [65]. Coherent LO phonons are investigated also in II–VI semiconductors and their nanostructures [66–71]. Below-bandgap excitation on ZnTe [66] and ZnSe [68] induces coherent phonons via ISRS, while TDFS dominates the coherent phonon generation for above-gap excitation on CdTe [69].

Recent development of ultrashort intense laser pulses has enabled the observation of small-amplitude, high-frequency phonons in wide-gap materials. Typical examples include diamond (Sect. 2.5.1), GaN [72], ZnO [73, 74], and TiO₂ [75, 76]. Onishi and coworkers observed the bulk and surface phonon modes of TiO₂ at four different frequencies in their TRSHG measurements

[75, 76]. When the surface was covered with trimethyl acetate (TMA), which has no resonance with the pump and probe wavelengths, no molecular vibration was observed. When adsorbates were replaced by *p*-nitrobenzoate (*p*NB), which has two-photon resonance, the SH intensity showed a modulation at a fifth frequency assigned as a molecular vibration [76]. The study thus provided a first successful application of TRSHG to organic adsorbates.

Systematic TRSHG studies on alkali-atom adsorbed metal surfaces by Matsumoto and coworkers provided a deep insight on how coherent motions are created under very different electronic configurations [15, 77, 78]. The results showed that the coherent phonon generation critically depends on the surface and bulk electronic structure of the substrate.

Coherent optical phonons can couple with localized excitations such as excitons and defect centers. For example, strong exciton–phonon coupling was demonstrated for lead phthalocyanine (PbPc) [79] and CuI [80] as an intense enhancement of the coherent phonon amplitude at the excitonic resonances. In alkali halides [81–83], nuclear wave-packets localized near F centers were observed as periodic modulations of the luminescence spectra.

Coherent phonons and phonon–polaritons were utilized not only to monitor the temperature-driven phase transitions [7, 8, 84–87] but also to investigate the photo-induced phase transitions (PIPT) in the strongly correlated systems in the real time. Photodoping of holes into VO₂ induced the insulator-to-metal transition, which exhibited a delay of several tens of fs associated with the phonon connecting the two crystallographic phases [88]. Optical measurements on perovskite manganite Pr_{0.7}Ca_{0.3}MnO₃ revealed a 31 THz oscillation that was suggestive of coherent orbital wave [89]. For one-dimensional extended Peierls–Hubbard system [Pd(chxn)₂Br]Br₂, photo-induced formation of Mott–Hubbard state was observed, followed by a coherent oscillation of the bridging-Br [90]. Organic conductors such as TTF-CA [91–93], K-TCNQ [94, 95], (EDO-TTF)₂PF₆ [96–98], and BEDT-TTF salt [99] are specifically under extensive investigation. Coherent oscillations due to dimerization of the molecules were observed during the photo-induced ionic-to-neutral and neutral-to-ionic transitions in TTF-CA, and was associated to the spin-Peierls instability [91, 92]. (EDO-TTF)₂PF₆ exhibited a nonequilibrium charge-disproportionate state upon photoexcitation, and the coherent intermolecular bending mode was observed at a frequency depending on the probe wavelength [96–98].

In a heavy fermion compound Yb₁₄MnSb₁₁, the dephasing rate of the coherent optical phonons decreased with lowering temperature above Curie temperature T_C , but increased below T_C . The results were attributed to the coupling between an optical phonon mode and the Kondo effect [100].

2.8 Concluding Remarks

In this chapter, we have reviewed the recent experimental researches on the coherent optical phonons using optical detection technique. Optical detection has great advantages in its experimental simplicity, higher time-resolution

and higher signal-to-noise ratio. The disadvantage is that the interpretation of the experimentally obtained quantity is not straightforward. Higher signal-to-noise ratio implies that it can probe lattice dynamics under a weak optical perturbation as well as an intense one. The extremely nonequilibrium phenomena under intense perturbation, including PIPT, are attractive in their own right. However, they are challenging targets because they are often associated with irreversible processes – which pump-probe scheme is not designed for. Even in group V semimetals, which are the model materials of coherent phonon studies, the lattice dynamics under intense excitation still lack a comprehensive understanding. We expect recent rapid developments in theoretical researches, in addition to systematic experimental studies, contribute to fully reveal the nonequilibrium phononic and electronic dynamics in solids.

References

1. S. De Silvestri, J.G. Fujimoto, E.P. Ippen, E.B. Gamble, L.R. Williams, K.A. Nelson, *Chem. Phys. Lett.* **116**(2–3), 146 (1985)
2. T.K. Cheng, S.D. Brorson, A.S. Kazeroonian, J.S. Moodera, G. Dresselhaus, M.S. Dresselhaus, E.P. Ippen, *Appl. Phys. Lett.* **57**(10), 1004 (1990)
3. G.C. Cho, W. Kütt, H. Kurz, *Phys. Rev. Lett.* **65**(6), 764 (1990)
4. J.M. Chwalek, C. Uher, J.F. Whitaker, G.A. Mourou, J.A. Agostineli, M. Lelental, *Appl. Phys. Lett.* **57**(16), 1696 (1990)
5. T. Dekorsy, W. Kutt, T. Pfeifer, H. Kurz, *Europhys. Lett.* **23**(3), 223 (1993)
6. M. Hase, K. Mizoguchi, H. Harima, S. Nakashima, M. Tani, K. Sakai, M. Hangyo, *Appl. Phys. Lett.* **69**(17), 2474 (1996)
7. R. Merlin, *Solid State Commun.* **102**(2–3), 207 (1997)
8. H.J. Bakker, S. Hunsche, H. Kurz, *Rev. Modern Phys.* **70**(2), 523 (1998)
9. T. Dekorsy, G.C. Cho, H. Kurz, in *Coherent Phonons in Condensed Media* ed. by M.Cardona, G. Güntherodt. Light Scattering in Solids VIII (Springer, Berlin, 2000), p. 169
10. M. Först, T. Dekorsy, *Coherent Phonons in Bulk and Low-Dimensional Semiconductors*, ed. by S. De Silvestri, G. Cerullo, G. Lanzani. Coherent Vibrational Dynamics (CRC, Boca Raton, 2007), p. 129
11. G. Lanzani, in *Coherent Phonon Dynamics in π -Conjugated Chains*, ed. by S. De Silvestri, G. Cerullo, G. Lanzani. Coherent Vibrational Dynamics (CRC, Boca Raton, 2007), p. 93
12. M. Gühr, in *Coherent Dynamics of Halogen Molecules in Rare Gas Solids*, ed. by S. De Silvestri, G. Cerullo, G. Lanzani. Coherent Vibrational Dynamics (CRC, Boca Raton, 2007), p. 173
13. S.L. Dexheimer, in *Coherent Vibrational Dynamics of Exciton Self-Trapping in Quasi-One-Dimensional Systems*, ed. by S. De Silvestri, G. Cerullo, G. Lanzani. Coherent Vibrational Dynamics (CRC, Boca Raton, 2007), p. 223
14. Y.-M. Chang, L. Xu, H.W.K. Tom, *Chem. Phys.* **251**(1–3), 283 (2000)
15. Y. Matsumoto, K. Watanabe, *Chem. Rev.* **106**(10), 4234 (2006)
16. A.V. Kuznetsov, C.J. Stanton, *Phys. Rev. Lett.* **73**(24), 3243 (1994)

17. T. Dekorsy, H. Auer, C. Waschke, H.J. Bakker, H.G. Roskos, H. Kurz, *Phys. Rev. Lett.* **74**(5), 738 (1995)
18. M. Tani, R. Fukasawa, H. Abe, S. Matsuura, K. Sakai, S. Nakashima, *J. Appl. Phys.* **83**(5), 2473 (1998)
19. L. Dhar, J. Rogers, K.A. Nelson, *Chem. Rev.* **94**, 157 (1994)
20. K.J. Yee, Y.S. Lim, T. Dekorsy, D.S. Kim, *Phys. Rev. Lett.* **86**(8), 1630 (2001)
21. K. Ishioka, M. Kitajima, O.V. Misochko, *J. Appl. Phys.* **103**, 123505 (2008)
22. Y.-M. Chang, *Appl. Phys. Lett.* **82**(11), 1781 (2003)
23. E.S. Zijlstra, L.L. Tatarinova, M.E. Garcia, *Phys. Rev. B* **74**(22), 220301 (2006)
24. T.K. Cheng, J. Vidal, H.J. Zeiger, G. Dresselhaus, M.S. Dresselhaus, E.P. Ippen, *Appl. Phys. Lett.* **59**(16), 1923 (1991)
25. K. Ishioka, M. Kitajima, O.V. Misochko, *J. Appl. Phys.* **100**, 093501 (2006)
26. G.A. Garrett, T.F. Albrecht, J.F. Whitaker, R. Merlin, *Phys. Rev. Lett.* **77**(17), 3661 (1996)
27. H.J. Zeiger, J. Vidal, T.K. Cheng, E.P. Ippen, G. Dresselhaus, M.S. Dresselhaus, *Phys. Rev. B* **45**(2), 768 (1992)
28. T.E. Stevens, J. Kuhl, R. Merlin, *Phys. Rev. B* **65**, 144304 (2002)
29. D.M. Riffe, A.J. Sabbah, *Phys. Rev. B* **76**(8), 085207 (2007)
30. T. Dekorsy, T. Pfeifer, W. Kütt, H. Kurz, *Phys. Rev. B* **47**(7), 3842 (1993)
31. G.C. Cho, H.J. Bakker, T. Dekorsy, H. Kurz, *Phys. Rev. B* **53**(11), 6904 (1996)
32. U. Bovensiepen, *J. Phys. Condens. Matter* **19**, 235417 (2007)
33. L. Min, R.J.D. Miller, *Appl. Phys. Lett.* **56**(6), 524 (1990)
34. Y.-M. Chang, L. Xu, H.W.K. Tom, *Phys. Rev. Lett.* **78**(24), 4649 (1997)
35. K. Sokolowski-Tinten, C. Blome, J. Blums, A. Cavalleri, C. Dietrich, A. Tarasevitch, I. Uschmann, E. Förster, M. Kammmer, M. Horn von Hoegen, D. von der Linde, *Nature* **422**(6929), 287 (2003)
36. M. Hase, M. Kitajima, S. Nakashima, K. Mizoguchi *Phys. Rev. Lett.* **88**(6), 067401 (2002)
37. M.F. DeCamp, D.A. Reis, P.H. Bucksbaum, R. Merlin, *Phys. Rev. B* **64**, 092301 (2001)
38. O.V. Misochko, K. Ishioka, M. Hase, M. Kitajima, *J. Phys. Condens. Matter* **19**(15), 156227 (2007)
39. E.D. Murray, D.M. Fritz, J.K. Wahlstrand, S. Fahy, D.A. Reis, *Phys. Rev. B* **72**, 060301(R) (2005)
40. E.D. Murray, S. Fahy, D. Prendergast, T. Ogitsu, D.M. Fritz, D.A. Reis, *Phys. Rev. B* **75**(18), 184301 (2007)
41. T. Dumitrica, *J. Phys. Condens. Matter* **19**, 181003 (2007)
42. O.V. Misochko, K. Ishioka, M. Hase, M. Kitajima, *J. Phys. Condens. Matter* **18**, 10571 (2006)
43. O.V. Misochko, M. Hase, K. Ishioka, M. Kitajima, *Phys. Rev. Lett.* **92**(19), 197401 (2004)
44. T. Baumert, M. Grosser, R. Thalweiser, G. Gerber, *Phys. Rev. Lett.* **67**(27), 3753 (1991)
45. M.J.J. Vrakking, D.M. Villeneuve, A. Stolow, *Phys. Rev. A* **54**(1), R37 (1996)
46. M.S. Diakhate, E.S. Zijlstra, M.E. Garcia, *Appl. Phys. A* **96**, 5177 (2009)
47. M. Hase, M. Kitajima, A.M. Constantinescu, H. Petek, *Nature* **426**, 51 (2003)
48. T. Pfeifer, W. Kütt, H. Kurz, R. Scholz, *Phys. Rev. Lett.* **69**(22), 3248 (1992)
49. M. Nakajima, H. Harima, K. Morita, K.M. Itoh, K. Mizoguchi, *Phys. Rev. B* **63**, 161304(R) (2001)

50. K. Ishioka, M. Hase, M. Kitajima, H. Petek, *Appl. Phys. Lett.* **89**, 231916 (2006)
51. K. Ishioka, M. Hase, M. Kitajima, L. Wirtz, A. Rubio, H. Petek, *Phys. Rev. B* **77**(12), 121402 (2008)
52. T. Mishina, K. Nitta, Y. Masumoto, *Phys. Rev. B* **62**(41), 2908 (2000)
53. R. Lu, K. Ishioka, O.V. Misochko, M. Hase, M. Kitajima, *Surf. Sci.* **593**(1-3), 116 (2005)
54. Y.-S. Lim, K.-J. Yee, J.-H. Kim, E.H. Haroz, J. Shaver, J. Kono, S.K. Doorn, R.H. Hauge, R.E. Smalley, *Nano Lett.* **6**(12), 2696 (2006)
55. A. Gambetta, C. Manzoni, E. Menna, M. Meneghetti, G. Cerullo, G. Lanzani, S. Tretiak, A. Piryatinski, A. Saxena, R.L. Martin, A.R. Bishop, *Nat. Phys.* **2**, 515 (2006)
56. M. Hase, K. Ishioka, J. Demsar, K. Ushida, M. Kitajima, *Phys. Rev. B* **71**(18), 184301 (2005)
57. M. Hase, J. Demsar, M. Kitajima, *Phys. Rev. B* **74**(21), 212301 (2006)
58. V.V. Kruglyak, R.J. Hicken, G.P. Srivastava, M. Ali, B.J. Hickey, A.T.G. Pym, B.K. Tanner, *Phys. Rev. B* **76**(1), 012301 (2007)
59. A. Melnikov, I. Radu, A. Povolotskiy, T. Wehling, A. Lichtenstein, U. Bovensiepen, *J. Phys. D Appl. Phys.* **41**(16), 164004 (2008)
60. A. Melnikov, I. Radu, U. Bovensiepen, O. Krupin, K. Starke, E. Matthias, M. Wolf, *Phys. Rev. Lett.* **91**, 227403 (2003)
61. U. Bovensiepen, A. Melnikov, I. Radu, O. Krupin, K. Starke, M. Wolf, E. Matthias, *Phys. Rev. B* **69**(23), 235417 (2004)
62. A. Melnikov, A. Povolotskiy, U. Bovensiepen, *Phys. Rev. Lett.* **100**(24), 247401 (2008)
63. Y.M. Chang, H.W. Chu, C.H. Shen, H.Y. Chen, S. Gwo, *Appl. Phys. Lett.* **90**(7), 72111 (2007)
64. Y.M. Chang, H.W. Lin, Y.L. Hong, S. Gwo, *J. Appl. Phys.* **104**(3), 036105 (2008)
65. M. Hase, *Appl. Phys. Lett.* **94**(11), 112111 (2009)
66. Y.-S. Lim, S.-C. Yoon, K.-J. Yee, J.-H. Lee, D.S. Kim, D. Lee, *Phys. Rev. B* **68**(15), 153308 (2003)
67. J.K. Wahlstrand, T.E. Stevens, J. Kuhl, R. Merlin, *Physica B* (**316–317**), 55 (2002)
68. Y.-S. Lim, S.-C. Yoon, K.-J. Yee, Y.-H. Ahn, E. Oh, J.-H. Lee, *Appl. Phys. Lett.* **82**(15), 2446 (2003)
69. K. Ishioka, M. Kitajima, J. Irisawa, Y. Hironaka, K. Ushida, K.G. Nakamura, *Jpn. J. Appl. Phys.* **45**(12), 9111 (2006)
70. A.V. Bragas, C. Aku-Leh, S. Costantino, A. Ingale, J. Zhao, R. Merlin, *Phys. Rev. B* **69**(20), 205306 (2004)
71. S. Tripathy, H.P. Wagner, A. Ueta, D. Hommel, *Phys. Rev. B* **75**(24), 245316 (2007)
72. K.J. Yee, K.G. Lee, E. Oh, D.S. Kim, *Phys. Rev. Lett.* **88**(10), 105501 (2002)
73. I.H. Lee, K.J. Yee, K.G. Lee, E. Oh, D.S. Kim, Y.S. Lim, *J. Appl. Phys.* **93**(8), 4939 (2003)
74. C. Aku-Leh, J. Zhao, R. Merlin, J. Menendez, M. Cardona, *Phys. Rev. B* **71**(20), 205211 (2005)
75. S. Fujiiyoshi, T. Ishibashi, H. Onishi, *J. Phys. Chem. B* **109**(18), 8557 (2005)
76. T. Nomoto, H. Onishi, *Chem. Phys. Lett.* **455**(4-6), 343 (2008)

77. K. Watanabe, N. Takagi, Y. Matsumoto, *Phys. Rev. B* **71**, 085414 (2005)
78. M. Fuyuki, K. Watanabe, D. Ino, H. Petek, Y. Matsumoto, *Phys. Rev. B* **76**(11), 115427 (2007)
79. K. Mizoguchi, S. Fujita, M. Nakayama, *Appl. Phys. A* **78**(4), 461 (2004)
80. O. Kojima, K. Mizoguchi, M. Nakayama, *J. Lumin.* **112**(1–4), 80 (2005)
81. T. Koyama, Y. Takahashi, M. Nakajima, T. Suemoto, *Phys. Rev. B* **73**(16), 161102 (2006)
82. T. Koyama, Y. Takahashi, M. Nakajima, T. Suemoto, *J. Chem. Phys.* **124**(22), 221104 (2006)
83. T. Koyama, Y. Takahashi, M. Nakajima, T. Suemoto, *Phys. Rev. B* **76**, 115122 (2007)
84. T. Kohmoto, K. Tada, T. Moriyasu, Y. Fukuda, *Phys. Rev. B* **74**(6), 64303 (2006)
85. O.V. Misochko, M. Tani, K. Sakai, K. Kisoda, S. Nakashima, V.N. Andreev, F.A. Chudnovsky, *Phys. Rev. B* **58**(19), 12789 (1998)
86. H.T. Kim, Y.W. Lee, B.J. Kim, B.G. Chae, S.J. Yun, K.Y. Kang, K.J. Han, K.J. Yee, Y.S. Lim, *Phys. Rev. Lett.* **97**(26), 266401 (2006)
87. H. Kamioka, S. Saito, M. Isobe, Y. Ueda, T. Suemoto, *Phys. Rev. Lett.* **88**(12), 127201/1 (2002)
88. A. Cavalleri, T. Dekorsy, H.H.W. Chong, J.C. Kieffer, R.W. Schoenlein, *Phys. Rev. B* **70**(16), 161102 (2004)
89. D. Polli, M. Rini, S. Wall, R.W. Schoenlein, Y. Tomioka, Y. Tokura, G. Cerullo, A. Cavalleri, *Nat. Mater.* **6**, 643 (2007)
90. H. Matsuzaki, M. Yamashita, H. Okamoto, *J. Phys. Soc. Jpn.* **75**(12), 123701/1 (2006)
91. S. Iwai, S. Tanaka, K. Fujinuma, H. Kishida, H. Okamoto, Y. Tokura, *Phys. Rev. Lett.* **88**(5), 057402 (2002)
92. H. Okamoto, Y. Ishige, S. Tanaka, H. Kishida, S. Iwai, Y. Tokura, *Phys. Rev. B* **70**(16), 165202 (2004)
93. K. Tanimura, *Phys. Rev. B* **70**(14), 144112 (2004)
94. H. Okamoto, K. Ikegami, T. Wakabayashi, Y. Ishige, J. Togo, H. Kishida, H. Matsuzaki, *Phys. Rev. Lett.* **96**(3), 037405 (2006)
95. K. Ikegami, K. Ono, J. Togo, T. Wakabayashi, Y. Ishige, H. Matsuzaki, H. Kishida, H. Okamoto, *Phys. Rev. B* **76**(8), 085106 (2007)
96. M. Chollet, L. Guerin, N. Uchida, S. Fukaya, H. Shimoda, T. Ishikawa, K. Matsuda, T. Hasegawa, A. Ota, H. Yamochi, G. Saito, R. Tazaki, S. Adachi, S. Koshihara, *Science* **307**(5706), 86 (2005)
97. K. Onda, S. Ogihara, T. Ishikawa, Y. Okimoto, X. Shao, H. Yamochi, G. Saito, S. Koshihara, *J. Phys. Condens. Matter* **20**(22), 224018 (2008)
98. K. Onda, S. Ogihara, K. Yonemitsu, N. Maeshima, T. Ishikawa, Y. Okimoto, X. Shao, Y. Nakano, H. Yamochi, G. Saito, S. Koshihara, *Phys. Rev. Lett.* **101**(6), 067403 (2008)
99. S. Iwai, K. Yamamoto, A. Kashiwazaki, F. Hiramatsu, H. Nakaya, Y. Kawakami, K. Yakushi, H. Okamoto, H. Mori, Y. Nishio, *Phys. Rev. Lett.* **98**(9), 097402 (2007)
100. K.S. Burch, E.M.C. Elbert, D. Talbayev, B.C. Sales, D. Mandrus, A.J. Taylor, R.D. Averitt, *Phys. Rev. Lett.* **100**(2), 026409 (2008)